

A Scalable Quantum Non-local Neural Network for Image Classification

Sparsh Gupta¹, Debanjan Konar², Vaneet Aggarwal²

¹Franklin W. Olin College of Engineering, Needham, MA 02492 USA

²Purdue University, West Lafayette, IN 47907 USA

sgupta1@olin.edu, dkonar@purdue.edu, vaneet@purdue.edu

Abstract

Non-local operations play a crucial role in computer vision enabling the capture of long-range dependencies through weighted sums of features across the input, surpassing the constraints of traditional convolution operations that focus solely on local neighborhoods. Non-local operations typically require computing pairwise relationships between all elements in a set, leading to quadratic complexity in terms of time and memory. Due to the high computational and memory demands, scaling non-local neural networks to large-scale problems can be challenging. This article introduces a hybrid quantum-classical scalable non-local neural network, referred to as Quantum Non-Local Neural Network (QNL-Net), to enhance pattern recognition. The proposed QNL-Net relies on inherent quantum parallelism to allow the simultaneous processing of a large number of input features enabling more efficient computations in quantum-enhanced feature space and involving pairwise relationships through quantum entanglement. We benchmark our proposed QNL-Net with other quantum counterparts to binary classification with datasets MNIST and CIFAR-10. The simulation findings showcase our QNL-Net achieves cutting-edge accuracy levels in binary image classification among quantum classifiers while utilizing fewer qubits.

Code — <https://anonymous.4open.science/r/QNL-Net/>

Introduction

Computer vision has become a cornerstone of artificial intelligence, consisting of a wide array of applications such as autonomous driving (Bao et al. 2023), medical imaging (Li et al. 2023), healthcare (Zhou et al. 2022), etc. An essential task in this domain is image classification, where the goal is to assign a label to an image based on its visual significance. This task also builds upon more complex applications such as image segmentation (Minaee et al. 2021), object detection (Amjoud and Amrouch 2023; Fu et al. 2023), and scene understanding (Naseer, Khan, and Porikli 2018). Image classification approaches have been significantly advanced by Convolutional Neural Networks (CNNs) (O’shea and Nash 2015), which achieve state-of-the-art performance on datasets like ImageNet (Krizhevsky, Sutskever, and Hinton 2012). However, CNNs are limited by their local receptive fields, which restricts them from capturing broader contextual information and long-range dependencies within an image. To overcome

these limitations, non-local neural networks were introduced to capture long-range dependencies in data, an extension of the self-attention mechanism used in Transformer architectures (Vaswani et al. 2017). Initially proposed for computer vision applications by (Wang et al. 2018), non-local neural networks capture global context effectively and have shown significant improvements in computer vision tasks that benefit from modeling long-range dependencies.

Parallel to these advancements, quantum machine learning (QML) (Biamonte et al. 2017) has emerged as a revolutionary technology built upon the principles of quantum mechanics, which describes the behavior and nature of atoms at the smallest fundamental level and applies them to machine learning. In classical computing, information only exists in bits, which are 0 or 1. In contrast, quantum computing introduces the concept of qubits that can have quantum states $|0\rangle$ and $|1\rangle$ simultaneously, taking advantage of the concept of superposition and introducing features such as quantum parallelism (Nielsen and Chuang 2001). Theoretically, this allows for speeding up computations and devising algorithms that can solve complex challenges more efficiently compared to classical computing where computation might be expensive and inefficient, and potentially revolutionize fields like pattern recognition and image classification, optimization (Abbas et al. 2023), cryptography (Bernstein and Lange 2017), etc. QML also introduces algorithms for classification problems such as QSVM, Quantum Kernel methods, Variational Quantum Classifiers (VQC), etc. VQC is a particularly interesting approach within QML because it lets us combine classical and quantum computing to use a quantum circuit as the core algorithm consisting of quantum gates that can be parameterized (Benedetti et al. 2019; Peddireddy, Bansal, and Aggarwal 2023). These parameters can be optimized using classical methods, enabling the model to be trained with a hybrid quantum-classical approach, which we utilize in our work. Researchers have still been trying to understand whether QML offers a significant advantage to classical machine learning theoretically and practically, and it has been an active field of research for long (Biamonte et al. 2017). A sub-domain in this field, Quantum Neural Networks (QNNs), has been developed intensively to determine whether these are capable of outperforming classical neural networks. It was also recently explored in (Abbas et al. 2021) by performing simulations on actual quantum hardware and proving

that QML does, in fact, offer several advantages. However, a few challenges exist due to insufficient capabilities for fault-tolerance, still-evolving quantum error correction techniques, and quantum scalability, which presents an avenue for revolutionary research in this field and transitioning to a new era of quantum computing from the present noisy intermediate-scale quantum (NISQ) era (Preskill 2018; Gujju, Matsuo, and Raymond 2024). The present challenges limit the practical applications of QML algorithms. Still, despite that, developing QML research and devising new quantum algorithms offers an outlet to test methodologies as a proof-of-concept on a smaller scale and deploy applications in the future while we approach scalable quantum processors.

In this context, our paper proposes a Quantum Non-local Neural Network (QNL-Net), which combines the principles of quantum computing with the non-local neural network mechanism. By leveraging quantum entanglement, the QNL-Net can establish non-local correlations between qubits, mimicking the behavior of classical non-local operations while exploiting the advantages of quantum mechanics to enhance machine learning performance and capabilities. This paper aims to improve pattern recognition and binary classification tasks in computer vision by capturing long-range dependencies more effectively. The main contributions of this paper are:

1. We introduce a scalable and customizable quantum implementation of the non-local neural network mechanism that utilizes only four qubits to achieve state-of-the-art performance on binary classification tasks in computer vision.
2. We also utilize classical machine learning techniques for dimensionality reduction of features before these are processed by the QNL-Net framework, therefore leveraging the advantages of hybrid quantum-classical machine learning models.
3. We comprehensively evaluate the QNL-Net's performance on benchmark datasets such as MNIST and CIFAR-10, showcasing its robustness to noise and its potential advantages over traditional quantum binary classification models. Our hybrid classical-quantum models, particularly the CNN-QNL-Net, achieved near-perfect binary classification accuracies on the MNIST dataset (99.96% test accuracy) and outperformed benchmark quantum classifiers such as QTN-VQC (98.6% with 12 qubits) (Qi, Yang, and Chen 2023) and Hybrid TTN-MERA (99.87% with 8 qubits) (Grant et al. 2018) using significantly fewer qubits, i.e., 4 qubits.

Related Work

Image classification using quantum machine learning (QML) became an area of significant interest due to its potential advantages over classical methods. One notable approach was Quantum Convolutional Neural Networks (QCNNs), which utilized quantum circuits to implement convolutional operations, focusing on quantum phase recognition and quantum error correction optimization techniques (Cong, Choi, and Lukin 2019). Another significant development was the Quanvolutional Neural Network, introduced by (Henderson et al.

2020) in 2019, which employed quantum convolution (quanvolutional) layers. These layers transformed classical data using random quantum circuits to extract features, akin to the feature extraction process in classical CNNs. Their results demonstrated superior accuracy and training performance compared to classical CNNs. QML models have also shown efficacy in binary classification tasks for noisy datasets and images (Schetakis et al. 2022). Additionally, recent work by (Cherrat et al. 2024) developed an approach for loading matrices as quantum states and introducing trainable quantum orthogonal layers adaptable to different quantum computer capabilities. This method yielded promising results on superconducting quantum computers.

Several works also explored the application of quantum neural networks for binary classification tasks in computer vision, providing benchmarks for our results. QTN-VQC (Qi, Yang, and Chen 2023) built a framework with quantum circuits for tensor-train networks integrated with variational quantum circuits for an efficient training pipeline. Another work introduced hierarchical quantum classifiers (Grant et al. 2018), which utilized several expressive circuits to classify highly entangled quantum states and demonstrated robustness to noise. A scalable approach for quantum neural networks (SQNNs) for classification was discussed in (Wu, Tao, and Li 2022), where authors proposed a strategy to use multiple small-scale quantum devices to extract local features and perform prediction over these collected features. (Jiang, Xiong, and Shi 2021) presented the QuantumFlow model, which represented data as unitary matrices to achieve quantum advantage, reducing the cost complexity of unitary matrices-based neural computation. These recent advancements in QML models demonstrated robustness in image classification, making them suitable for handling higher-dimensional data more effectively than their classical counterparts.

Non-local Neural Networks

Traditional convolution operations in convolutional neural networks (CNNs), a popular choice for computer vision models, process a local neighborhood, and applying these operations repeatedly to capture long-range dependencies causes incremental growth in the receptive field. This has several drawbacks associated with computational inefficiency and difficulties in optimization. Non-local neural networks address these limitations by introducing non-local operations that compute the response at a position as a weighted sum of the features at all positions in the input. These are simple operations that are highly efficient and generic in capturing long-range dependencies, which is of utmost importance in computer vision (Wang et al. 2018).

A generic non-local operation for an input signal's (image, sequence, video) feature map $x \in \mathbb{R}^{N \times C}$, where N is the number of positions (i.e. pixels) and C is the number of channels, can be defined as:

$$y_i = \frac{1}{C(x)} \sum_{\forall j} f(x_i, x_j)g(x_j), \quad (1)$$

where i is the index of an output position (in space/time/spacetime) whose response is to be computed, j enumerates

over all possible positions, and y is the output signal. f is a pairwise function that computes a scalar representing the relationship (such as similarity) between i and all j . g is a unary function that computes a representation of the input signal at j and normalizes it by a factor $\mathcal{C}(x)$.

In terms of the functions, g is simply considered as a linear embedding such that $g(x_i) = W_g x_j$, where W_g is a learned weight matrix. There are several choices for the pairwise function f such as:

1. Gaussian:

$$f(x_i, x_j) = e^{x_i^T x_j}, \mathcal{C}(x) = \sum_{\forall j} f(x_i, x_j);$$

2. Embedded Gaussian:

$$f(x_i, x_j) = e^{\theta(x_i)^T \phi(x_j)}, \mathcal{C}(x) = \sum_{\forall j} f(x_i, x_j);$$

where $\theta(x_i) = W_\theta x_i$ and $\phi(x_j) = W_\phi x_j$ are linear embeddings. This also relates to self-attention (as explored in (Vaswani et al. 2017)), which non-local networks are just an extension of in the computer vision domain, or more specifically, a generic space or spacetime domain. This is due to the fact that for any i , $\frac{1}{\mathcal{C}(x)} f(x_i, x_j)$ becomes the softmax computation along the dimension j .

3. Dot Product:

$$f(x_i, x_j) = \theta(x_i)^T \phi(x_j), \mathcal{C}(x) = N;$$

where N is the number of positions in x .

4. Concatenation:

$$f(x_i, x_j) = \text{ReLU}(w_f^T [\theta(x_i)^T, \phi(x_j)]), \mathcal{C}(x) = N;$$

A non-local block in spacetime encapsulates the non-local operation in eq.(1) elegantly and can be defined as:

$$z_i = W_i y_i + x_i \quad (2)$$

where y_i is the non-local operation and residual connection ‘+ x_i ’ allows integrating the non-local block into any pre-trained model without disruptions in their initial behavior (He et al. 2016).

Quantum Non-local Neural Network

In this work, we introduce the Quantum Non-Local Neural Network (QNL-Net), which utilizes trainable quantum circuits to implement non-local operations, effectively capturing and processing long-range dependencies in input data. The QNL-Net module integrates with classical dimensionality reduction techniques to function as a hybrid quantum-classical classifier. In this section, we first delve into the design and implementation of the QNL-Net module. Next, we discuss the integration of classical dimensionality reduction techniques with the QNL-Net to create a hybrid classifier, highlighting the CNN-QNL-Net and PCA-QNL-Net models. Finally, we cover the post-QNL-Net classical computation.

The QNL-Net mechanism translates classical non-local operations into quantum circuits, enabling the network to exploit the parallelism and entanglement properties of quantum computing. This translation involves designing quantum gates

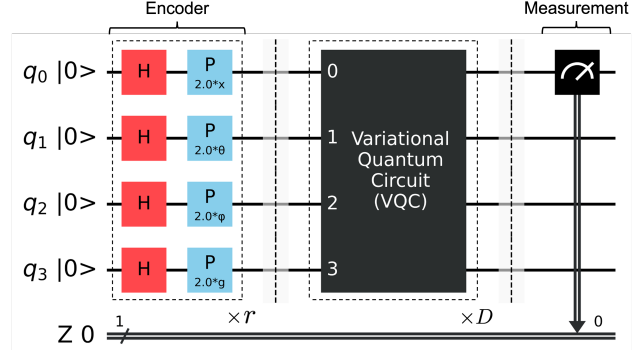


Figure 1: The Quantum Non-local Neural Network (QNL-Net) mechanism’s four-qubit circuit composed of three parts: (i) Encoder: uses Qiskit’s ZFeatureMap (Kanazawa et al. 2023) to encode classical data into quantum states. (ii) Variational Quantum Circuit (VQC): the classically trainable quantum circuit. (iii) Measurement: the circuit is measured at qubit 0 in the Pauli-Z basis. The encoder and the VQC ansatz have a depth of r and D respectively.

and circuits that can replicate the functionality of classical non-local layers, allowing the network to analyze complex data structures more efficiently. To encode the classical data $\mathcal{X} \in \mathbb{R}^d$ into the quantum space where $\mathcal{X} = [y_0, y_1, \dots, y_k]$, we utilize Qiskit’s ZFeatureMap (Kanazawa et al. 2023) (as one can see in Fig. 1) which takes advantage of the quantum-enhanced feature space, providing a quantum advantage to classification problems (Havlíček et al. 2019). The feature map Φ acts as $\Phi : \mathcal{X} \rightarrow |\psi_\Phi\rangle$, where the feature space $|\psi_\Phi\rangle$ is an n -qubit Hilbert space, such that

$$|\psi_\Phi\rangle = (U_\Phi(y_k) H^{\otimes n})^r |0^n\rangle, \quad 0 \leq k \leq N - 1, \quad (3)$$

where r is the depth or the number of repetitions of the feature map, $H^{\otimes n}$ is a layer of Hadamard gates acting on all n qubits, and N denotes the number of input vectors in a data sample. U_Φ is the encoding ansatz used in the feature map composed of single-qubit phase-shift (P_λ) gates for rotation about the Z -axis,

$$U_\Phi(\mathcal{X}) = \bigotimes_{k=1}^n P_{2*y_k}. \quad (4)$$

We utilize variational quantum circuits in this mechanism, which can be trained classically to optimize trainable parameters using a predefined cost function (Benedetti et al. 2019). This hybrid quantum-classical approach leverages the expressive power of quantum circuits while making use of classical optimization techniques for efficient parameter tuning. We implement three different ansatzes with five parameterized rotation gates in each, enabling fine-grained control over the quantum state. These three ansatz each have three CX gates with distinct configurations, introducing entanglement-induced correlations between the qubits and ensuring that the quantum state captures the non-local dependencies in the data. The quantum circuits for the ansatzes are presented in Fig. 2.

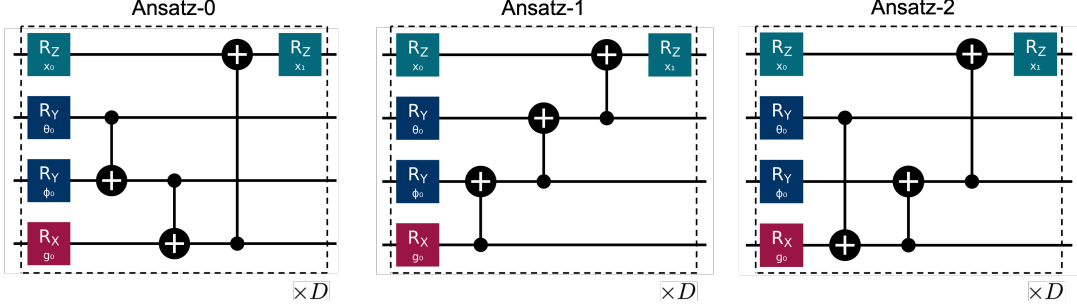


Figure 2: The three ansatzes used as the variational quantum circuits (VQCs) in the QNL-Net mechanism. R_x , R_y , R_z rotation gates represent single-qubit rotations along the x , y , z -axes respectively with trainable parameters. The specific strategies for performing entanglement using CX gates are: cyclic pattern (Ansatz-0), reverse linear chain (Ansatz-1), and a mixed pattern (Ansatz-2).

We initially apply rotation gates to each qubit in all the ansatzes to obtain the following quantum state.

$$|\psi_1\rangle = R_z(x_0)_{q_0} R_y(\theta_0)_{q_1} R_y(\phi_0)_{q_2} R_x(g_0)_{q_3} |\psi_\Phi\rangle \quad (5)$$

The variation in the ansatzes comes from different entanglement strategies described below. The configurations ensure that all qubits are entangled with each other in order to capture the non-local dependencies throughout the circuit. In Ansatz-0, the CX gates form a cyclic pattern, creating a loop of entanglement among the qubits. Ansatz-1's CNOT gates form a reverse linear chain, creating a backward sequential entanglement. Ansatz-2 forms a non-linear and unique mixed pattern entanglement strategy using the CNOT gates. The resultant quantum states for the respective ansatz are as follows.

$$|\psi_2^{[0]}\rangle = CX_{q_1q_2} CX_{q_2q_3} CX_{q_3q_0} |\psi_1\rangle, \quad (6)$$

$$|\psi_2^{[1]}\rangle = CX_{q_3q_2} CX_{q_2q_1} CX_{q_1q_0} |\psi_1\rangle, \quad (7)$$

$$|\psi_2^{[2]}\rangle = CX_{q_1q_3} CX_{q_3q_2} CX_{q_2q_0} |\psi_1\rangle. \quad (8)$$

Then, we add our final rotation gate on qubit 0 in each ansatz, and obtain the following quantum state.

$$|\psi_3^{[a]}\rangle = R_z(x_1)_{q_0} |\psi_2^{[a]}\rangle, \quad (9)$$

where a represents the desired ansatz and $a = 0, 1$, or 2 . This sequence of gates and entanglements in the ansatzes constitutes one layer of the respective ansatz and can also be represented by the unitary operator, such that,

$$U_a(\theta) = |\psi_3^{[a]}\rangle. \quad (10)$$

Now, each layer can be applied for a depth of D to enhance the expressiveness of the model, and therefore, we obtain the final state of the circuit,

$$|\psi_{final}\rangle = (U_a(\theta))^D |\psi_\Phi\rangle, \quad (11)$$

where a is the desired ansatz $a = 0, 1$, or 2 . According to the Born rule, measuring any quantum state in the Pauli- Z basis (σ_z) either collapses into the state $|0\rangle$ with probability $|\alpha|^2$ or

into the state $|1\rangle$ with probability $|\beta|^2$ (Nielsen and Chuang 2001). In general, the expectation of any observable \hat{O} for a state $|\psi\rangle$ can be denoted as

$$\langle \hat{O} \rangle = \langle \psi | \hat{O} | \psi \rangle = \sum_i m_i p_i \quad (12)$$

where m_i are the possible measurement values, i.e., the eigenvalues weighted by their respective probabilities $p_i = |\alpha|^2 - |\beta|^2$. Therefore, to measure an observable O on n -qubits, we can also represent it as a sum of tensor products of Pauli operators, such that,

$$O = \sum_{k=1}^K \alpha_k P_k, \quad \alpha_k \in \mathbb{R}, \quad (13)$$

where $P_k \in \{I, X, Y, Z\}^{\otimes n}$ denotes a Pauli observable. In our mechanism, we measure the circuit in the Pauli- Z computational basis at only one qubit, q_0 , whereas the rest of the qubits are measured using an Identity (I) operation. So, we can denote the measurement of q_0 for an input state of $|\psi_\Phi\rangle$ as $\langle Z_x \rangle_\Phi$, where x is the data embedding on qubit q_0 , and

$$\langle Z_x \rangle_\Phi = \langle \psi_\Phi | U_x^\dagger(\theta_x) Z_1 U_x(\theta_x) | \psi_\Phi \rangle, \quad (14)$$

where θ_x is a parameter on the quantum ansatz U_x and Z_1 represents Pauli- Z measurement on the first qubit. It has been shown in recent years that the integration of classical and quantum mechanisms for machine learning is very promising as these hybrid models leverage the strengths of both paradigms. Classical models perform best with feature extraction and dimensionality reduction problems, while quantum models offer superior capabilities by using quantum mechanical phenomena such as entanglement and superposition, enabling the extraction of exponentially more information out of each chunk of data (Biamonte et al. 2017; Huang et al. 2022). Therefore, this hybrid approach can lead to more effective machine learning systems, particularly for tasks involving pattern recognition in large and complex datasets. In this work, we employ two hybrid classical-quantum non-local neural network (QNL-Net) models: CNN-QNL-Net and PCA-QNL-Net, as seen in Fig. 3. The primary purpose for using these classical models is for dimensionality and feature

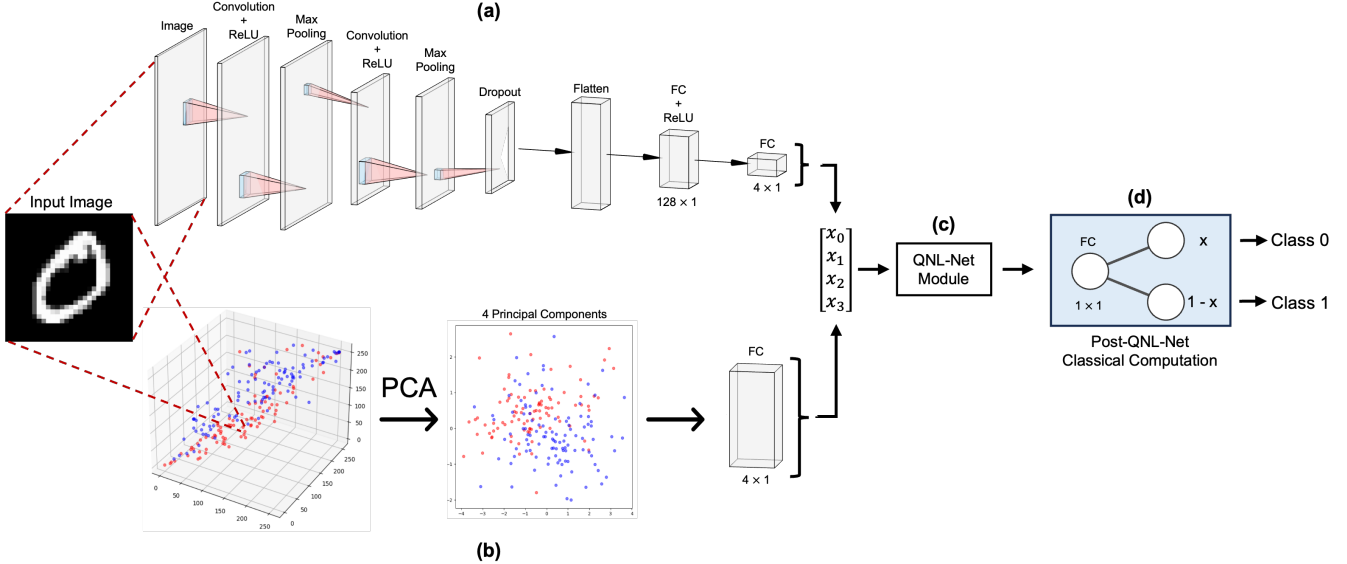


Figure 3: The pipeline for the Hybrid Classical-QNL-Net Models used in this work: (a) CNN-QNL-Net: Two convolutional layers with ReLU activation and max pooling extract features from input images, followed by a dropout layer and flattening of the features, and then two fully connected (FC) layers to prepare the data for the QNL-Net module. (b) PCA-QNL-Net: PCA reduces the input data dimensionality to 4 components, which are then processed by a fully connected (FC) layer before being fed into the QNL-Net module. (c) QNL-Net: The quantum part of the pipeline which performs computation on the four features obtained from the classical models according to the mechanism and outputs a single measurement obtained from qubit 0. (d) Post-QNL-Net Classical Computation: A fully connected layer is used to fine-tune the quantum output, and then this output is transformed and concatenated as desired for binary classification.

reduction, transforming input data into a feature vector of size 4×1 , such that each value of the vector can be encoded into one qubit of the QNL-Net layer to capture and analyze long-range dependencies and intricate patterns among these features.

After measuring the output from the QNL-Net, we perform further classical computation by adding a fully connected layer consisting of a single learnable parameter, which helps fine-tune and optimize the quantum output and improve the model’s performance. The linear transformation performed by this layer is as follows.

$$x = W_4 Q + b_4, \quad (15)$$

where $Q \in \mathbb{R}^1$ is the single QNL-Net output, $W_4 \in \mathbb{R}^{1 \times 1}$ is the weight matrix, and $b_4 \in \mathbb{R}^1$ is the bias vector. Finally, for performing binary classification, we compute the complement of the probabilities and concatenate them together to obtain a single vector compatible for loss computation and backpropagation,

$$\hat{y} = \text{cat}(x, 1 - x), \quad (16)$$

where $\hat{y} \in \mathbb{R}^2$ is the resultant vector containing the predicted probabilities for both classes.

Quantum Simulation

Datasets

In our experiments, we utilize two widely used image processing datasets for image classification: MNIST (Deng 2012)

and CIFAR-10 (Krizhevsky, Hinton et al. 2009) (sample images are shown in the Appendix in Fig. 5). For MNIST, we focus on binary classification using the digits 0 and 1, comprising 12,665 training samples and 2,115 testing samples. For CIFAR-10, we perform binary classification using classes 2 (birds) and 8 (ships). Before feeding the images into the models, we normalize them using the global mean and standard deviation of each dataset, scaling pixel values from [0, 255] to [0, 1].

Simulation Settings

The experiments are conducted on a MacBook Pro with an M2 Max chip and 64GB RAM. The QNL-Net network is implemented by utilizing the EstimatorQNN module of Qiskit Machine Learning 0.7.2 and Qiskit 1.1.0, which facilitates the encoding of classical data into quantum data and enables the training of the ansatz. The classical node is constructed, and gradient optimization is performed using PyTorch 2.3.0, which connects seamlessly with the EstimatorQNN module. The models are trained for 100 epochs with a batch size of 1 using the negative log-likelihood (NLL) loss function for convergence. The Adam optimizer (Kingma and Ba 2014) is configured with different learning rates, which vary between 0.0001 to 0.0004 depending upon the model and the ansatz used as listed in Appendix Table 1. The ExponentialLR scheduler (Li and Arora 2019) uses a γ decay rate of 0.9. The rest of the parameters are set to default.

Simulation Results

The experiments were conducted using different combinations of feature map repetitions $r = 1, 2$, or 3 and the number of ansatz repetitions $D = 1, 2$ or 3 . The accuracies reported are averaged for all runs for each specific ansatz and model configuration, as shown in Appendix Table 1.

The results on the MNIST dataset for classes 0 and 1 indicate that the CNN-QNL-Net model performs slightly better than the PCA-QNL-Net model, achieving a near-perfect average classification test accuracy of 99.96% whereas the PCA-QNL-Net achieved a test accuracy of 99.59%. Ansatz-0 and Ansatz-2 generally yield better results compared to Ansatz-1 for this dataset, as evident in Appendix Table 1. For the CIFAR-10 dataset, the hybrid-QNL-Net models perform comparatively worse than the MNIST due to the introduction of three color channels (i.e., RGB) compared to MNIST’s grayscale images. However, the CNN-QNL-Net was still able to obtain an average test accuracy of 93.98%. Ansatz-1 performs better on the testing dataset for CIFAR-10 compared to the other ansatzes. On both datasets, the CNN-QNL-Net significantly outperforms the PCA-QNL-Net due to its ability to efficiently extract features from the dataset before feeding them to the QNL-Net module.

Increasing the depth of both the feature map and the ansatzes (i.e., r and D , respectively) generally improved classification accuracies due to the increased expressiveness of the circuit. However, it also resulted in longer training times compared to using fewer repetitions, which still obtained reasonably good results within the bounds reported in Appendix Table 1. Furthermore, PCA-QNL-Net models required higher learning rates to obtain convergence than the CNN-QNL-Net models. The PCA-QNL-Net demonstrated faster training compared to the CNN-QNL-Net, as CNNs add an overhead for training parameters, utilizing a total of 34,282 classical parameters on MNIST and 41,314 classical parameters on CIFAR-10. The PCA-QNL-Net, however, optimizes only 22 classical parameters from the linear layers, offering an advantage in terms of classical training efficiency.

Table 1 presents the complete results for all different ansatz and models run on the datasets. Further, Table 2 compares the results from our models to the benchmark quantum binary classifiers discussed in the Related Work. Our hybrid classical-quantum models, particularly the CNN-QNL-Net, outperform the benchmark models across both datasets. This superior performance underscores the effectiveness of combining classical convolutional networks with quantum neural network layers, enabling more robust and accurate classification. For the MNIST dataset, Figure 4a shows that the PCA-QNL-Net model achieves a lower final loss compared to the CNN-QNL-Net model across all ansatz configurations, suggesting that the PCA-QNL-Net model fits the training data more closely by the end of the training period. Despite this, the CNN-QNL-Net model reaches higher training accuracy more quickly than the PCA-QNL-Net model, as shown in Figure 4c, indicating better generalization. In contrast, on the CIFAR-10 dataset, the CNN-QNL-Net model demonstrates a more rapid decrease in training loss and achieves a lower final loss value compared to the PCA-QNL-Net model (Fig. 4b). This suggests faster convergence and a better fit to

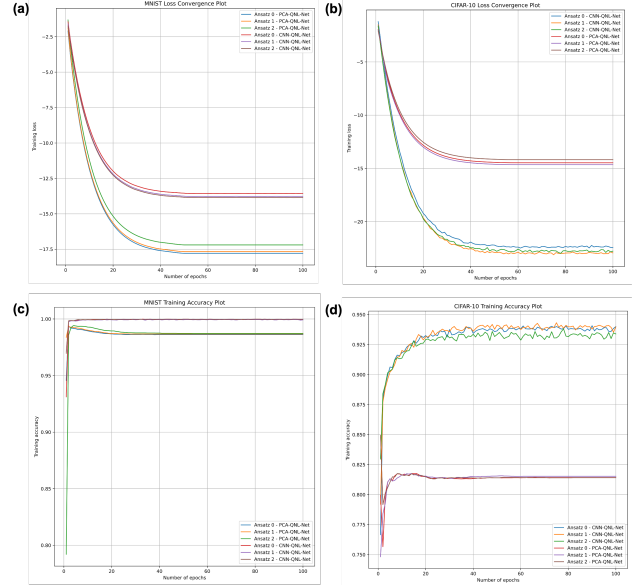


Figure 4: Training loss convergence and accuracy plots for CNN-QNL-Net and PCA-QNL-Net models using three ansatzes with one feature map repetition ($r = 1$) and one ansatz repetition ($D = 1$). (a) and (b) show loss convergence during training for the MNIST dataset (classes 0 and 1) and the CIFAR-10 dataset (classes 2 and 8), respectively. (c) and (d) display training accuracy on the respective datasets.

the CIFAR-10 training data. The CNN-QNL-Net model also consistently achieves higher training accuracy faster than the PCA-QNL-Net model in Fig. 4d, reinforcing its effectiveness in learning from more complex data. Overall, our experimental results confirm that integrating quantum circuits with classical neural network architectures significantly enhances model performance, setting a new benchmark in quantum machine learning.

Discussion

The novelty of the QNL-Net architecture lies in its efficient utilization of fewer qubits, a critical consideration in the NISQ era. However, its significance extends beyond that to take into account the fundamental principles of quantum mechanics, particularly in its treatment of rotations around axes and entanglement. The choice of rotation gates in the QNL-Net ansatzes is tied to the fundamental idea behind non-local neural networks, which aim to capture intricate spatial dependencies within the data. In the quantum paradigm, rotation gates achieve this by translating quantum states around different axes, thereby implementing spatial transformations. Now, for simplification, consider the raw data x and the three embeddings (θ, ϕ, g) in the non-local neural net architecture as akin to the four features passed on to the QNL-Net circuit. In non-local neural nets, raw data is not embedded, but in this work, we utilize rotation around the z -axis primarily because it allows us to maintain a trainable parameter on qubit 0 after the feature map encoding which ensures the consistency and completeness of quantum theory while not affecting the

Table 1: This table summarizes the performance metrics of various configurations of the QNL-Net model on binary classification tasks across datasets: MNIST digits 0 and 1 and CIFAR-10 classes 2 (bird) and 8 (ship). The configurations vary by the ansatz type, the model used (CNN-QNL-Net or PCA-QNL-Net), and the learning rate. The reported metrics include the average training accuracy and test accuracy across different variations of the number of repetitions of the feature map (r) and the number of repetitions of the ansatz (D). Numbers following \pm represent the standard deviation across configurations.

Dataset	Ansatz	Model	Learning Rate	Average Train Accuracy (%)	Average Test Accuracy (%)
MNIST (0, 1)	0	CNN-QNL-Net	1×10^{-4}	99.97 \pm 0.02	99.96 \pm 0.03
	1	CNN-QNL-Net	1×10^{-4}	99.96 \pm 0.02	99.95 \pm 0.02
	2	CNN-QNL-Net	1×10^{-4}	99.96 \pm 0.03	99.95 \pm 0.04
	0	PCA-QNL-Net	1.5×10^{-4}	99.65 \pm 0.17	99.54 \pm 0.16
	1	PCA-QNL-Net	1.5×10^{-4}	99.24 \pm 0.19	99.18 \pm 0.34
	2	PCA-QNL-Net	1.5×10^{-4}	99.67 \pm 0.23	99.59 \pm 0.21
CIFAR-10 (2, 8)	0	CNN-QNL-Net	3×10^{-4}	94.20 \pm 0.77	93.54 \pm 0.66
	1	CNN-QNL-Net	3×10^{-4}	94.13 \pm 0.45	93.98 \pm 0.37
	2	CNN-QNL-Net	3×10^{-4}	94.21 \pm 0.32	93.76 \pm 0.14
	0	PCA-QNL-Net	4×10^{-4}	81.94 \pm 1.51	81.16 \pm 1.09
	1	PCA-QNL-Net	4×10^{-4}	81.79 \pm 0.34	80.95 \pm 0.35
	2	PCA-QNL-Net	4×10^{-4}	81.67 \pm 0.73	80.86 \pm 0.74

Table 2: This table compares the performance of our QNL-Net model with other benchmark quantum classifiers on binary classification tasks using the MNIST dataset. The CNN-QNL-Net model demonstrates better results using significantly fewer qubits.

Model	Classes	Qubits	Test Accuracy
QTN-VQC (Qi, Yang, and Chen 2023)	0, 1	12	98.6
Hybrid TTN-MERA (Grant et al. 2018)	0, 1	8	99.87 \pm 0.02
CNN-QNL-Net [ours]	0, 1	4	99.96 \pm 0.03
SQNN (Wu, Tao, and Li 2022)	3, 6	64	97.47
QF-hNet-BN (Jiang, Xiong, and Shi 2021)	3, 6	12	98.27
CNN-QNL-Net [ours]	3, 6	4	99.94 \pm 0.02

measurement initially. The R_y gates around qubits 1 and 2 for embeddings θ and ϕ , respectively, is crucial. These gates induce phase shifts in the states of the corresponding qubits, playing a vital role in generating interference effects and complex quantum states. Additionally, they facilitate capturing relative phase information, which is pivotal in discerning subtle patterns within the data. The linear embedding g translates to qubit 3, where an R_x gate modifies the probability amplitudes of states $|0\rangle$ and $|1\rangle$, fine-tuning the data representation within the quantum circuit.

A key advantage of QNL-Net is leveraging quantum entanglement. While classical non-local blocks typically involve matrix multiplications within the embeddings and element-wise summation with the raw data, the QNL-Net utilizes the intrinsic significance of CNOT entanglements to replicate variable dependencies present in classical non-local mechanisms. This creates a highly interconnected system between all qubits, effectively extracting intricate probabilities and facilitating the exploration of complex data structures in a quantum framework. As we can infer from the results, it does not matter significantly what the specific pattern for entanglement is in different ansatz, rather the idea that all qubits encompassing different rotations are entangled together. Then, further applying another R_z gate on qubit 0, which is already in a highly entangled state, introduces additional phase modulation within the entangled system. This modulation is crucial for fine-tuning the quantum state before measurement, thereby influencing the outcome probabilities.

Despite the promising results obtained from these models,

several limitations were identified. The current implementation is restricted by the reliance on classical computing methods that might be computationally inefficient as the datasets become much more extensive and the models are more complex. Still, it is a trade-off we must consider as we utilize lesser quantum resources. Multi-class classification posed a particular challenge as it performed poorly, likely due to the small circuit size with Pauli-Z measurement at only one qubit, which limits the model's capability in distinguishing between multiple classes. Additionally, the model's performance could be further validated by testing on more diverse and larger datasets and exploring the effects of different quantum encodings and variational circuit designs.

Nevertheless, the implications of this research extend to various practical applications. In fields like image classification, medical imaging, and real-time video analysis, efficiently capturing long-range dependencies using quantum-enhanced models can lead to significant advancements in accuracy and performance. Furthermore, the scalable nature of QNL-Net suggests that as quantum hardware evolves, these models could be deployed in real-world scenarios, providing a competitive edge over traditional classical approaches.

Conclusion

This paper introduced the Quantum Non-local Neural Networks (QNL-Net) mechanism as a novel hybrid classical-quantum approach for image classification. Through experiments on MNIST and CIFAR-10 datasets, QNL-Net models demonstrated competitive performance in binary classification tasks, using fewer qubits compared to traditional quantum classifiers. The use of fundamental quantum techniques like entanglement and rotation gates proved effective in capturing intricate spatial dependencies critical for image analysis.

However, QNL-Net exhibits limitations in multi-class classification and efficiency with larger, complex datasets due to reliance on classical preprocessing methods. These challenges underscore the need to explore future work on innovative QNL-Net variants and optimization techniques. Additionally, exploring the integration of more efficient quantum encoding strategies might also enhance performance.

In conclusion, QNL-Net promises advancements in accuracy and efficiency for image classification tasks, with potential transformative impacts in fields requiring robust pattern recognition, such as medical imaging and real-time video analysis. Its ability to operate with reduced computational resources compared to classical and existing quantum methods positions QNL-Net as a scalable solution for quantum-enhanced machine learning applications, laying the groundwork for broader use in practical applications.

References

Abbas, A.; Ambainis, A.; Augustino, B.; Bärtschi, A.; Buhrman, H.; Coffrin, C.; Cortiana, G.; Dunjko, V.; Egger, D. J.; Elmegreen, B. G.; et al. 2023. Quantum optimization: Potential, challenges, and the path forward. *arXiv preprint arXiv:2312.02279*.

Abbas, A.; Sutter, D.; Zoufal, C.; Lucchi, A.; Figalli, A.; and Woerner, S. 2021. The power of quantum neural networks. *Nature Computational Science*, 1(6): 403–409.

Amjoud, A. B.; and Amrouch, M. 2023. Object detection using deep learning, CNNs and vision transformers: A review. *IEEE Access*, 11: 35479–35516.

Bao, F.; Wang, X.; Sureshbabu, S. H.; Sreekumar, G.; Yang, L.; Aggarwal, V.; Boddeti, V. N.; and Jacob, Z. 2023. Heat-assisted detection and ranging. *Nature*, 619(7971): 743–748.

Benedetti, M.; Lloyd, E.; Sack, S.; and Fiorentini, M. 2019. Parameterized quantum circuits as machine learning models. *Quantum Science and Technology*, 4(4): 043001.

Bernstein, D. J.; and Lange, T. 2017. Post-quantum cryptography. *Nature*, 549(7671): 188–194.

Biamonte, J.; Wittek, P.; Pancotti, N.; Rebentrost, P.; Wiebe, N.; and Lloyd, S. 2017. Quantum machine learning. *Nature*, 549(7671): 195–202.

Brunton, S. L.; and Kutz, J. N. 2022. *Data-driven science and engineering: Machine learning, dynamical systems, and control*. Cambridge University Press.

Cherrat, E. A.; Kerenidis, I.; Mathur, N.; Landman, J.; Strahm, M.; and Li, Y. Y. 2024. Quantum vision transformers. *Quantum*, 8: 1265.

Cong, I.; Choi, S.; and Lukin, M. D. 2019. Quantum convolutional neural networks. *Nature Physics*, 15(12): 1273–1278.

Deng, L. 2012. The mnist database of handwritten digit images for machine learning research [best of the web]. *IEEE signal processing magazine*, 29(6): 141–142.

Fu, X.; Zhou, F.; Peddireddy, D.; Kang, Z.; Jun, M. B.-G.; and Aggarwal, V. 2023. An finite element analysis surrogate model with boundary oriented graph embedding approach for rapid design. *Journal of Computational Design and Engineering*, 10(3): 1026–1046.

Grant, E.; Benedetti, M.; Cao, S.; Hallam, A.; Lockhart, J.; Stojevic, V.; Green, A. G.; and Severini, S. 2018. Hierarchical quantum classifiers. *npj Quantum Information*, 4(1): 65.

Guju, Y.; Matsuo, A.; and Raymond, R. 2024. Quantum machine learning on near-term quantum devices: Current state of supervised and unsupervised techniques for real-world applications. *Physical Review Applied*, 21(6): 067001.

Havlíček, V.; Córcoles, A. D.; Temme, K.; Harrow, A. W.; Kandala, A.; Chow, J. M.; and Gambetta, J. M. 2019. Supervised learning with quantum-enhanced feature spaces. *Nature*, 567(7747): 209–212.

He, K.; Zhang, X.; Ren, S.; and Sun, J. 2016. Deep residual learning for image recognition. In *Proceedings of the IEEE conference on computer vision and pattern recognition*, 770–778.

Henderson, M.; Shakya, S.; Pradhan, S.; and Cook, T. 2020. Quanvolutional neural networks: powering image recognition with quantum circuits. *Quantum Machine Intelligence*, 2(1): 2.

Huang, H.-Y.; Broughton, M.; Cotler, J.; Chen, S.; Li, J.; Mohseni, M.; Neven, H.; Babbush, R.; Kueng, R.; Preskill, J.; et al. 2022. Quantum advantage in learning from experiments. *Science*, 376(6598): 1182–1186.

Jiang, W.; Xiong, J.; and Shi, Y. 2021. A co-design framework of neural networks and quantum circuits towards quantum advantage. *Nature communications*, 12(1): 579.

Jolliffe, I. T.; and Cadima, J. 2016. Principal component analysis: a review and recent developments. *Philosophical transactions of the royal society A: Mathematical, Physical and Engineering Sciences*, 374(2065): 20150202.

Kanazawa, N.; Egger, D. J.; Ben-Haim, Y.; Zhang, H.; Shanks, W. E.; Aleksandrowicz, G.; and Wood, C. J. 2023. Qiskit experiments: A python package to characterize and calibrate quantum computers. *Journal of Open Source Software*, 8(84): 5329.

Kingma, D. P.; and Ba, J. 2014. Adam: A method for stochastic optimization. *arXiv preprint arXiv:1412.6980*.

Kocsis, P.; Súkeník, P.; Brasó, G.; Nießner, M.; Leal-Taixé, L.; and Elezi, I. 2022. The unreasonable effectiveness of fully-connected layers for low-data regimes. *Advances in Neural Information Processing Systems*, 35: 1896–1908.

Krizhevsky, A.; Hinton, G.; et al. 2009. Learning multiple layers of features from tiny images. <https://www.cs.toronto.edu/~kriz/cifar.html>.

Krizhevsky, A.; Sutskever, I.; and Hinton, G. E. 2012. Imagenet classification with deep convolutional neural networks. *Advances in neural information processing systems*, 25.

Li, M.; Jiang, Y.; Zhang, Y.; and Zhu, H. 2023. Medical image analysis using deep learning algorithms. *Frontiers in Public Health*, 11: 1273253.

Li, Z.; and Arora, S. 2019. An exponential learning rate schedule for deep learning. *arXiv preprint arXiv:1910.07454*.

Minaee, S.; Boykov, Y.; Porikli, F.; Plaza, A.; Kehtarnavaz, N.; and Terzopoulos, D. 2021. Image segmentation using deep learning: A survey. *IEEE transactions on pattern analysis and machine intelligence*, 44(7): 3523–3542.

Mitarai, K.; Negoro, M.; Kitagawa, M.; and Fujii, K. 2018. Quantum circuit learning. *Physical Review A*, 98(3): 032309.

Naseer, M.; Khan, S.; and Porikli, F. 2018. Indoor scene understanding in 2.5/3d for autonomous agents: A survey. *IEEE access*, 7: 1859–1887.

Nielsen, M. A.; and Chuang, I. L. 2001. *Quantum computation and quantum information*, volume 2. Cambridge university press Cambridge.

O’shea, K.; and Nash, R. 2015. An introduction to convolutional neural networks. *arXiv preprint arXiv:1511.08458*.

Peddireddy, D.; Bansal, V.; and Aggarwal, V. 2023. Classical simulation of variational quantum classifiers using tensor rings. *Applied Soft Computing*, 141: 110308.

Preskill, J. 2018. Quantum computing in the NISQ era and beyond. *Quantum*, 2: 79.

Qi, J.; Yang, C.-H.; and Chen, P.-Y. 2023. Qtn-vqc: An end-to-end learning framework for quantum neural networks. *Physica Scripta*, 99(1): 015111.

Schetakis, N.; Aghamalyan, D.; Griffin, P.; and Boguslavsky, M. 2022. Review of some existing QML frameworks and novel hybrid classical–quantum neural networks realising binary classification for the noisy datasets. *Scientific reports*, 12(1): 11927.

Schuld, M.; Bergholm, V.; Gogolin, C.; Izaac, J.; and Killoran, N. 2019. Evaluating analytic gradients on quantum hardware. *Physical Review A*, 99(3): 032331.

Srivastava, N.; Hinton, G.; Krizhevsky, A.; Sutskever, I.; and Salakhutdinov, R. 2014. Dropout: a simple way to prevent neural networks from overfitting. *The journal of machine learning research*, 15(1): 1929–1958.

Vaswani, A.; Shazeer, N.; Parmar, N.; Uszkoreit, J.; Jones, L.; Gomez, A. N.; Kaiser, Ł.; and Polosukhin, I. 2017. Attention is all you need. *Advances in neural information processing systems*, 30.

Wang, X.; Girshick, R.; Gupta, A.; and He, K. 2018. Non-local neural networks. In *Proceedings of the IEEE conference on computer vision and pattern recognition*, 7794–7803.

Wu, J.; Tao, Z.; and Li, Q. 2022. wpScalable quantum neural networks for classification. In *2022 IEEE International Conference on Quantum Computing and Engineering (QCE)*, 38–48. IEEE.

Zhou, G.; Aggarwal, V.; Yin, M.; and Yu, D. 2022. A computer vision approach for estimating lifting load contributors to injury risk. *IEEE Transactions on Human-Machine Systems*, 52(2): 207–219.

Supplementary Material: Technical Appendix

Background on Quantum Computing

Quantum computing leverages the fundamentals of quantum mechanics, such as superposition and entanglement, to introduce new properties to computing. It uses the concept of qubits that have the computational basis states $|0\rangle$ and $|1\rangle$, which can also be represented as

$$|0\rangle = \begin{bmatrix} 1 \\ 0 \end{bmatrix}, |1\rangle = \begin{bmatrix} 0 \\ 1 \end{bmatrix}. \quad (17)$$

A qubit is a linear combination of these basis states, which is the general principle of superposition, and can be represented as a vector in a two-dimensional complex Hilbert space, such that,

$$|\psi\rangle = \alpha|0\rangle + \beta|1\rangle, \quad (18)$$

where $\alpha, \beta \in \mathbb{C}$ are the complex coefficients of the quantum states $|0\rangle$ and $|1\rangle$ respectively. The probabilities of the qubit being in state $|0\rangle$ or $|1\rangle$ are given by the magnitude squared of these coefficients $|\alpha|^2$ and $|\beta|^2$. These probability amplitudes satisfy the normalization condition $|\alpha|^2 + |\beta|^2 = 1$.

Entanglement is another quantum phenomenon where the states of two or more qubits become interconnected, and the state of one qubit affects the other entangled qubits. This also demonstrates that the states cannot be factored into a product of individual qubit states as they are strongly correlated (i.e., $|\psi_{AB}\rangle \neq |\psi_A\rangle \otimes |\psi_B\rangle$ for states A and B).

The first step to any quantum computation is encoding classical data into quantum states. To achieve this, several fundamental encoding techniques are used: (i) Basis encoding maps classical bits 0 and 1 to states $|0\rangle$ and $|1\rangle$ directly, and therefore each classical bit string is encoded as the corresponding quantum state; (ii) Amplitude encoding uses the amplitudes of a quantum state to represent classical data such that the sum of the squared amplitudes of the quantum state is normalized to 1 for the classical data; (iii) Phase encoding maps classical information to the phases of a quantum state and is used in the proposed QNL-Net mechanism.

Quantum computations are performed primarily by manipulating quantum states through unitary transformations, achieved using quantum gates. Hadamard (H) gate is used to attain an equal superposition of the two basis states. The H gate maps the basis state $|0\rangle$ to $\frac{|0\rangle+|1\rangle}{\sqrt{2}}$ and the basis state $|1\rangle$ to $\frac{|0\rangle-|1\rangle}{\sqrt{2}}$. Rotation gates (R_x, R_y, R_z) rotate the state of a qubit around a specified axis on the Bloch sphere. A Phase (P) gate shifts the phase of a qubit by a specified angle ϕ such that applying $P(\phi)$ to $|\psi\rangle$ in eq.(18) results in $P(\phi)|\psi\rangle = \alpha|0\rangle + \beta e^{i\phi}|1\rangle$. A CNOT (CX gate) is a two-qubit gate that flips the state of the second qubit (target) only if the first qubit (control) is $|1\rangle$. The following are the matrix representations of the relevant gates utilized in this work:

$$H = \frac{1}{\sqrt{2}} \begin{bmatrix} 1 & 1 \\ 1 & -1 \end{bmatrix}, \quad P(\phi) = \begin{bmatrix} 1 & 0 \\ 0 & e^{i\phi} \end{bmatrix}, \quad (19)$$

$$R_x(\theta) = \begin{bmatrix} \cos(\frac{\theta}{2}) & -i \sin(\frac{\theta}{2}) \\ -i \sin(\frac{\theta}{2}) & \cos(\frac{\theta}{2}) \end{bmatrix}, \quad (20)$$

$$R_y(\theta) = \begin{bmatrix} \cos(\frac{\theta}{2}) & -\sin(\frac{\theta}{2}) \\ \sin(\frac{\theta}{2}) & \cos(\frac{\theta}{2}) \end{bmatrix}, \quad (21)$$

$$R_z(\theta) = \begin{bmatrix} e^{-i\frac{\theta}{2}} & 0 \\ 0 & e^{i\frac{\theta}{2}} \end{bmatrix}, \quad CX = \begin{bmatrix} 1 & 0 & 0 & 0 \\ 0 & 1 & 0 & 0 \\ 0 & 0 & 0 & 1 \\ 0 & 0 & 1 & 0 \end{bmatrix}. \quad (22)$$

CNN-QNL-Net

We use the Convolutional Neural Network (CNN) architecture in combination with our QNL-Net Module because CNN is adept at capturing spatial dependencies and identifying local patterns within complex image data through convolutional and pooling layers, which reduce the input dimensionality while retaining essential features (O’shea and Nash 2015). In the proposed CNN-QNL-Net architecture, we start with two convolutional layers, each with an activation function and max pooling, for an input image tensor $X \in \mathbb{R}^{W \times H \times C}$, where W is the width, H is the height, and C is the number of channels (i.e. 1 for grayscale images and 3 for RGB images) of the input image. In general, mathematically, a convolution operation ‘*’ for an input image I and a filter K to output a feature map F looks like,

$$F[i, j] = (I * K)_{[i, j]}, \quad (23)$$

$$F[i, j] = \sum_{m=0}^{M-1} \sum_{n=0}^{N-1} \sum_{c=0}^{C-1} I_{[i+m, j+n, c]} \cdot K_{[m, n, c]}, \quad (24)$$

where i, j are positions in the output feature map F , m, n are positions in the filter K for channel c , and M, N , and C are the width, height, and number of channels of the filter respectively. The first convolutional layer applies a 2D convolution operation with K_1 filters (or kernels) of size 5×5 resulting in K_1 output channels, and is defined as,

$$Y_{[k]} = \sum_{c=1}^C X_{[c]} * W_{[k]} + b_{[k]}, \quad k = 1, \dots, K_1, \quad (25)$$

where $W_{[k]}$ is the k -th filter weight and $b_{[k]}$ is the bias term. We apply the activation function $ReLU$, which simply eliminates the negative values in an input vector and is defined as $ReLU(x) = \max(0, x)$, on each filter element-wise such that,

$$A_{[k]} = ReLU(Y_{[k]}), \quad A \in \mathbb{R}^{W_1 \times H_1 \times K_1}, \quad (26)$$

where W_1 and H_1 are the width and height after convolution. Then, we apply a max pooling operation with a pool size of 2×2 on the Convolution + ReLU layer to obtain the pooled tensor P , which reduces the spatial dimensions of

each channel by selecting the maximum value within each pool, such that,

$$P_{[k]} = \text{MaxPool}(A_{[k]}), \quad P \in \mathbb{R}^{W_2 \times H_2 \times K_1}, \quad (27)$$

where $W_2 = \frac{W_1}{2}$ and $H_2 = \frac{H_1}{2}$. This Convolution + ReLU + MaxPool layer combination is repeated again on P for further feature reduction with K_2 filters of size 5×5 , and we obtain,

$$Z_{[k]} = \sum_{c=1}^{K_1} P_{[c]} * W_{[k]} + b_{[k]}, \quad k = 1, \dots, K_2; \quad (28)$$

$$B_{[k]} = \text{ReLU}(Z_{[k]}), \quad B \in \mathbb{R}^{W_3 \times H_3 \times K_2}, \quad (29)$$

where W_3 and H_3 are the width and height after the second convolution. Again, we apply the max pooling operation with a pool size of 2×2 on the previous layer,

$$Q_{[k]} = \text{MaxPool}(B_{[k]}), \quad Q \in \mathbb{R}^{W_4 \times H_4 \times K_2}, \quad (30)$$

where $W_4 = \frac{W_3}{2}$ and $H_4 = \frac{H_3}{2}$. We apply a Dropout layer (Srivastava et al. 2014) to the resultant pooled tensor Q to prevent overfitting which sets any element of the input to 0 during training with probability p , such that,

$$D = \text{Dropout}(Q, p), \quad p = 0.5. \quad (31)$$

Then, we flatten the output D to obtain a 1-dimensional vector F of size $(W_4 \cdot H_4 \cdot K_2) \times 1$. We apply a fully-connected (FC) layer to this flattened vector F with ReLU activation, which results in,

$$H_1 = \text{ReLU}(W_1 F + b_1), \quad H_1 \in \mathbb{R}^{128 \times 1}, \quad (32)$$

where W_1 is the weight matrix and b_1 is the bias vector. FC layers simply apply a linear transformation to an input vector, essential for dimensionality reduction, aggregating scattered patterns across the features, and optimizing parameters (Kocsis et al. 2022). Further, applying a non-linear activation function (e.g., ReLU) to a linear transformation enables representing non-linear relationships within the data. Finally, to obtain an output vector H_2 with size 4×1 , which can be passed to the QNL-Net module, we apply our last FC layer to the output of H_1 such that,

$$H_2 = W_2 H_1 + b_2, \quad H_2 \in \mathbb{R}^{4 \times 1}, \quad (33)$$

where W_2 is the weight matrix and b_2 is the bias vector.

PCA-QNL-Net

Principal Component Analysis is another linear dimensionality reduction technique that is suitable for linearly separable datasets used in this study. It uses Singular Value Decomposition (SVD) of the data to project it to a lower dimensional space. PCA proves to be computationally efficient and easy to compute compared to a technique like CNN. It does provide some disadvantages by losing some patterns and information in the data when reducing its dimensionality (Jolliffe and Cadima 2016). In the PCA-QNL-Net architecture, our input data matrix is $X \in \mathbb{R}^{N \times P}$, where N is the number of samples in the dataset and P is the total number of pixels per

image. Before applying the SVD, the input data is centered for each feature, such that,

$$\mu = \frac{1}{N} \sum_{i=1}^N X_i, \quad (34)$$

$$\bar{X} = X - 1_N \mu^T, \quad (35)$$

where μ is the calculated mean vector of the data, 1_N is an N -dimensional vector of ones, and \bar{X} is the centered input data matrix. We perform SVD on this centered matrix to decompose it into several component matrices with various interesting properties (Brunton and Kutz 2022),

$$\bar{X} = U \Sigma W^T, \quad (36)$$

where $U \in \mathbb{R}^{N \times N}$ is a matrix with each of its columns being a length- N orthogonal unit vector or the left singular vector of X , $\Sigma \in \mathbb{R}^{N \times P}$ is a diagonal matrix composed of singular values of X , and $W \in \mathbb{R}^{P \times P}$ is a matrix with each of its columns being a length- P orthogonal unit vector or the right singular vector of X . We project the centered data matrix onto the principal components by selecting the desired L number of columns (or principal components, i.e., 4 in this case) of W , such that,

$$Z = \bar{X} W_L, \quad (37)$$

where $Z \in \mathbb{R}^{N \times L}$ is the desired reduced form of the data. This matrix is standardized to have zero mean and unit variance,

$$\bar{Z} = \frac{Z - \mu_z}{\sigma_z}, \quad (38)$$

where μ_z and σ_z are the mean and standard deviation of Z respectively. \bar{Z} is a reduced vector of size $L \times 1$ (i.e. 4×1) and is then passed to a fully connected layer, such that,

$$H_3 = W_3 \bar{Z} + b_3, \quad (39)$$

where W_3 is the weight matrix and b_3 is the bias vector. Finally, $H_3 \in \mathbb{R}^{4 \times 1}$ can be fed directly to the QNL-Net for further processing.

Loss Convergence Analysis

In the QNL-Net framework, a hybrid gradient backpropagation approach is used to train our model effectively. This approach comprises optimizing both the classical parameters in neural nets and the set of trainable parameters, which are the angles of quantum gates in VQCs. This hybrid training approach first applies a forward pass to optimize parameters and converge the loss function. Our model uses the negative log-likelihood (NLL) loss function for the binary classification problem. The NLL loss measures the variation between the true labels y and the classical predicted probabilities $\hat{y} = [\hat{y}_0, \hat{y}_1] = p(y|x; \theta)$ obtained from the measurement of the hybrid classical-QNL-Net model, and is defined for binary classification as:

$$\mathcal{L}(\theta, \phi) = - \sum_{i=1}^n (y_i \log \hat{y}_{i1} + (1 - y_i) \log \hat{y}_{i0}), \quad (40)$$

where n is the number of samples in the dataset, \hat{y}_0 is the predicted probability for class 0, \hat{y}_1 is the predicted probability for class 1, θ are the quantum parameters, and ϕ are the classical parameters.

To optimize both classical and quantum parameters, we compute the gradients of the loss with respect to the predicted probabilities,

$$\frac{\partial \mathcal{L}}{\partial \hat{y}_{i1}} = -\frac{y_i}{\hat{y}_{i1}}, \quad \frac{\partial \mathcal{L}}{\partial \hat{y}_{i0}} = -\frac{1-y_i}{\hat{y}_{i0}}. \quad (41)$$

Then, we compute the gradient of the predicted probabilities with respect to the quantum parameters using the parameter-shift rule (Mitarai et al. 2018; Schuld et al. 2019) to obtain,

$$\frac{\partial \hat{y}_{i1}}{\partial \theta_j} = \frac{p(y_i|x; \theta_j + \frac{\pi}{2}) - p(y_i|x; \theta_j - \frac{\pi}{2})}{2}. \quad (42)$$

Now, we can derive the gradient of the loss function with respect to the quantum parameters from eq.(41) & (42), such that,

$$\frac{\partial \mathcal{L}}{\partial \theta_j} = \sum_i \left(\frac{\partial \mathcal{L}}{\partial \hat{y}_{i1}} \frac{\partial \hat{y}_{i1}}{\partial \theta_j} + \frac{\partial \mathcal{L}}{\partial \hat{y}_{i0}} \frac{\partial \hat{y}_{i0}}{\partial \theta_j} \right). \quad (43)$$

For the classical parameters, we calculate the gradients of the predicted probabilities using standard backpropagation techniques,

$$\frac{\partial \mathcal{L}}{\partial \phi} = \sum_i \left(\frac{\partial \mathcal{L}}{\partial \hat{y}_{i1}} \frac{\partial \hat{y}_{i1}}{\partial h_i} + \frac{\partial \mathcal{L}}{\partial \hat{y}_{i0}} \frac{\partial \hat{y}_{i0}}{\partial h_i} \right) \frac{\partial h_i}{\partial \phi}, \quad (44)$$

where h denotes the output from the classical model. These derived first-order objective functions are optimized using the stochastic gradient descent method, Adam (Kingma and Ba 2014). The first-order moment m_t and the second-order moment for the quantum gradient (from eq.(43)) are estimated using the following equations,

$$m_t = \beta_1 m_{t-1} + (1 - \beta_1) \frac{\partial \mathcal{L}}{\partial \theta_j}, \quad (45)$$

$$v_t = \beta_2 v_{t-1} + (1 - \beta_2) \left(\frac{\partial \mathcal{L}}{\partial \theta_j} \right)^2, \quad (46)$$

where t is the iteration/time-step and constants β_1 & β_2 are the exponential decay rate. These moments are corrected for initialization bias and we obtain bias-corrected moments, such that,

$$\hat{m}_t = \frac{m_t}{1 - \beta_1^t}, \quad \hat{v}_t = \frac{v_t}{1 - \beta_2^t}. \quad (47)$$

Then, the parameters are updated accordingly,

$$\theta_j \leftarrow \theta_j - \eta \frac{\hat{m}_t}{\sqrt{\hat{v}_t} + \epsilon}, \quad (48)$$

where η is the learning rate and ϵ is an added small constant for numerical stability. The optimization process is similar to the above for classical parameters ϕ for the classical gradient in eq.(44).

We also utilize the ExponentialLR scheduler (Li and Arora 2019) to adjust the learning rate η after every epoch t for faster convergence to obtain,

$$\eta_{new} = \eta \cdot \gamma^t, \quad (49)$$

where η_{new} is the updated learning rate and γ is the decay rate.

Datasets

MNIST (Deng 2012) is a handwritten digit recognition dataset used for many machine learning and computer vision tasks. Each image in MNIST is a grayscale 28 x 28-pixel representation of handwritten digits ranging from 0 to 9. The MNIST dataset contains 60,000 training samples used to train models and 10,000 testing samples used to evaluate model performance. These samples are handwritten by various individuals, covering a lot of variations and styles, ideal for machine learning.

CIFAR-10 (Krizhevsky, Hinton et al. 2009) is another widely-used benchmark dataset in the field of computer vision. It presents a collection of 32 x 32 size RGB images distributed across ten classes, including images of objects such as airplanes, cars, birds, cats, etc. The dataset contains a total of 50,000 training samples (5000 training samples per class) and 10,000 testing samples (1000 testing samples per class). Its diverse set of classes, coupled with variations in lighting, angle, and pose within images, makes it a suitable dataset for evaluating the robustness and generalization capability of image classification models.



Figure 5: Sample images from the datasets used in this work: (a) MNIST (Deng 2012) classes 0 and 1; and (b) CIFAR-10 (Krizhevsky, Hinton et al. 2009) classes 2 and 8, i.e., bird and ship respectively.